NEW MULTI-BLOCK COMPUTATIONAL METHODOLOGY BY CHARACTERISTIC INTERFACE CONDITIONS WITH HIGH-ORDER INTERPOLATION

Takahiro Sumi*, Takuji Kutotaki ** and Jun Hiyama**
***Tottori University, Japan, ****Japan Aerospace Exploration Agency, Japan**

Keywords: *Interface conditions, Characteristics, Interpolation, Multi-block, High-order computation*

Abstract

In the previous study, the authors proposed the generalized characteristic interface conditions (GCIC) for high-order finite difference multi-block computation on structured grids. The GCIC can realize non-overlapped connection between adjacent sub-domains (blocks) and allows metric discontinuities on the interface boundary, however, the grid lines must be continuous on the interface. In this study, in order to enhance the flexibility of the GCIC, by incorporating the high-order interpolation method such as the Lagrange or B-spline interpolation, the GCIC+I (GCIC with interpolation) are newly developed and proposed. The GCIC+I can realize discontinuous grid line connection on the interface boundary, and the grid spatial resolution can be arbitrarily changed in each sub-domain. In this article, their theoretical concept is briefly presented, and suitable numerical test analysis is conducted in order to validate the proposed theory. As a result, successful functions of the GCIC+I are confirmed.

1 Introduction

Technical methodologies for high-order computations typical of the large eddy simulations (LES) and the direct numerical simulations (DNS) have been widely studied and applied to quantitative predictions of unsteady aerodynamic phenomena such as turbulent boundary layer transitions, aero-acoustic noises, etc. In these fields, high-order finite difference methods (FDM) on structured grids are mainly employed, because their order of accuracy and spatial resolution are easily controllable, however, most of their applications are limited in simple geometries. In curvilinear coordinates around complex geometry, construction of ideal smooth structured grids is generally difficult task, because metric continuities cannot be ensured perfectly in the whole computational domain, and as a result, numerical instabilities may be observed around the singular points.

As one of the promising candidates solving the above problem, overset grid methods can be taken into account. Sherer et al. have proposed a high-order finite-difference overset algorism on the structured grids. [1] They employ high-order finite difference schemes and high-order interpolation methods, and investigate their capabilities in detail. However, the overset grid methods essentially have difficulty and complexity on domain arrangements and numerical procedures especially in 3D problems.

On the other hand, the authors have proposed another multi-block computational methodology with the generalized characteristic interface conditions (GCIC). [2] By the application of the GCIC, the decomposed sub-domains are not overlapped but are connected on the grid points of the interface using inviscid characteristic relations straightforwardly derived from flow transport equations. Therefore, spatial differentiations are independently performed in each isolated sub-domain and do not cross the interface, which results in avoiding numerical oscillations. By the present, the authors have confirmed that the GCIC demonstrate excellent performances in practical multi-block computations around complex geometries. However, even if the metric discontinuities on the interface can be allowed, discontinuities of the grid lines cannot be essentially treated, and

which constraint still restricts efficiencies of the multi-block computations.

The aim of this study is theoretical extension of the GCIC so that the grid line discontinuities on the interface can be treated. Therefore, high-order interpolation methods are introduced and incorporated into the GCIC. Namely, the GCIC+I (GCIC with interpolation) are newly proposed. The main feature of the present concept is that the inviscid characteristics are interpolated on the interface with high-order accuracy and connected by the relations of the GCIC. The GCIC+I allow not only the metric discontinuities but also the grid line discontinuities on the block interface, and realize effective zonal grid refinements on structured grids.

2 GCIC

The theoretical details of the GCIC are described in the Ref. [2]. In this section, the conceptual overview is shortly presented. The upper side of Fig. 1 shows a 2D singular structured grid as a single domain. On the points represented by the black circles, grid lines are continuous but those metrics at the left side limit and those at the right side limit are discontinuous. In order to solve this problem, as shown in the lower side of Fig. 1, the single computational domain is decomposed into two sub-domains along the singular line, and proper characteristic-based interface conditions are imposed on the interface.

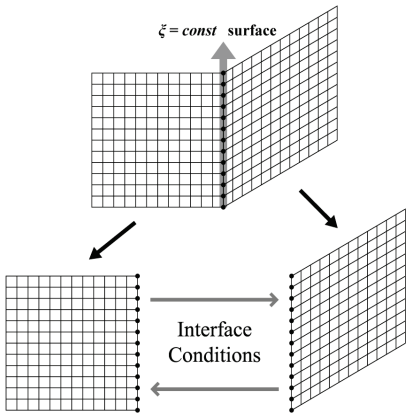

Fig 1. A single domain with metric discontinuities (upper), and two decomposed domains with interface conditions (lower).

Generally, the 3D Navier-Stokes equations can be expressed in the following non-conservative form with respect to ξ-direction normal to the interface:

$$\frac{\partial \boldsymbol{U}}{\partial t}+\xi_x\frac{\partial \boldsymbol{E}}{\partial \xi}+\xi_y\frac{\partial \boldsymbol{F}}{\partial \xi}+\xi_z\frac{\partial \boldsymbol{G}}{\partial \xi}+\boldsymbol{D}=0. \tag{1}$$

where, the inviscid flux derivative terms of the other directions and all the viscous flux derivative terms are involved in the source variable vector $\boldsymbol{D}$. In order to advance the characteristic analysis, the following two kinds of the Jacobian matrices are defined and introduced in terms of the conservative variable vector $\boldsymbol{U}$, primitive variable vector $\boldsymbol{V}$ and characteristic variable vector $\boldsymbol{W}$:

$$\underline{P}:=\frac{\partial \boldsymbol{U}}{\partial \boldsymbol{V}},\quad \underline{S}:=\frac{\partial \boldsymbol{V}}{\partial \boldsymbol{W}}. \tag{2}$$

Then, Eq. (1) can be rewritten as follows:

$$\frac{\partial \boldsymbol{U}}{\partial t}+\underline{P}\underline{S}\boldsymbol{L}+\boldsymbol{D}=0. \tag{3}$$

where, $\boldsymbol{L}$ is a characteristic wave amplitude variation vector and is defined as follows:

$$\begin{aligned}\boldsymbol{L}&=\underline{\Lambda}\underline{S}^{-1}\underline{P}^{-1}\frac{\partial \boldsymbol{U}}{\partial \xi}\\&=\underline{S}^{-1}\underline{P}^{-1}\left(\xi_x\frac{\partial \boldsymbol{E}}{\partial \xi}+\xi_y\frac{\partial \boldsymbol{F}}{\partial \xi}+\xi_z\frac{\partial \boldsymbol{G}}{\partial \xi}\right).\end{aligned} \tag{4}$$

where, $\underline{\Lambda}=\mathrm{diag}[U,U,U,U+C,U-C]$ is a diagonal matrix of eigenvalues of the inviscid flux derivative term in ξ-direction. The GCIC are derived from an intuitive fact that the time derivative of the conservative variable vector at upstream limit (subscript 'u') and that at downstream limit (subscript 'd') on the interface are strictly matched. From Eq. (3), these conditions are replaced by the spatial relations and are simply expressed as follows:

$$\begin{aligned}\left(\frac{\partial \boldsymbol{U}}{\partial t}\right)_{\mathrm{u}}=\left(\frac{\partial \boldsymbol{U}}{\partial t}\right)_{\mathrm{d}}&\Leftrightarrow\\ \underline{P}_{\mathrm{u}}\underline{S}_{\mathrm{u}}\boldsymbol{L}_{\mathrm{u}}+\boldsymbol{D}_{\mathrm{u}}&=\underline{P}_{\mathrm{d}}\underline{S}_{\mathrm{d}}\boldsymbol{L}_{\mathrm{d}}+\boldsymbol{D}_{\mathrm{d}},\end{aligned} \tag{5}$$

and can be arranged as the following two kind forms:

$$\begin{aligned} \boldsymbol{L}_{\mathrm{u}} &= \underline{S}_{\mathrm{u}}^{-1}\left[\underline{S}_{\mathrm{d}}\boldsymbol{L}_{\mathrm{d}} + \underline{P}_{\mathrm{u}}^{-1}\left(\boldsymbol{D}_{\mathrm{d}} - \boldsymbol{D}_{\mathrm{u}}\right)\right], \\ \boldsymbol{L}_{\mathrm{d}} &= \underline{S}_{\mathrm{d}}^{-1}\left[\underline{S}_{\mathrm{u}}\boldsymbol{L}_{\mathrm{u}} + \underline{P}_{\mathrm{d}}^{-1}\left(\boldsymbol{D}_{\mathrm{u}} - \boldsymbol{D}_{\mathrm{d}}\right)\right]. \end{aligned} \tag{6}$$

where, $\underline{P}_{\mathrm{u}} = \underline{P}_{\mathrm{d}}$ is obviously employed because their components are composed of only the primitive variables. [2] According to signs of the diagonal components of $\underline{\Lambda}$, the known $\boldsymbol{L}$ components in each side are directly calculated using Eq. (4), and on the contrary, the unknown ones are solved using Eq. (6) in consideration of characteristic interactions between the adjacent sub-domains. Generally, the latter manipulation contains an analytical matrix inversion. Consequently, the inviscid term normal to the interface is modified as follows:

$$\begin{aligned} \left(\xi_x\frac{\partial \boldsymbol{E}}{\partial \xi} + \xi_y\frac{\partial \boldsymbol{F}}{\partial \xi} + \xi_z\frac{\partial \boldsymbol{G}}{\partial \xi}\right)_{\mathrm{u}} &= \underline{P}_{\mathrm{u}}\underline{S}_{\mathrm{u}}\boldsymbol{L}_{\mathrm{u}}^{*}, \\ \left(\xi_x\frac{\partial \boldsymbol{E}}{\partial \xi} + \xi_y\frac{\partial \boldsymbol{F}}{\partial \xi} + \xi_z\frac{\partial \boldsymbol{G}}{\partial \xi}\right)_{\mathrm{d}} &= \underline{P}_{\mathrm{d}}\underline{S}_{\mathrm{d}}\boldsymbol{L}_{\mathrm{d}}^{*}. \end{aligned} \tag{7}$$

Then, a certain proper time integration scheme can be applied and the solutions are updated on the interface in the same procedure as inner points of the sub-domains:

$$\begin{aligned} \left(\frac{\partial \boldsymbol{U}}{\partial t}\right)_{\mathrm{u}}^{*} &= -\underline{P}_{\mathrm{u}}\underline{S}_{\mathrm{u}}\boldsymbol{L}_{\mathrm{u}}^{*} - \boldsymbol{D}_{\mathrm{u}}, \\ \left(\frac{\partial \boldsymbol{U}}{\partial t}\right)_{\mathrm{d}}^{*} &= -\underline{P}_{\mathrm{d}}\underline{S}_{\mathrm{d}}\boldsymbol{L}_{\mathrm{d}}^{*} - \boldsymbol{D}_{\mathrm{d}}. \end{aligned} \tag{8}$$

After the time integration, the primitive variables are averaged arithmetically to compress numerical round-off errors:

$$\boldsymbol{V}_{\mathrm{u}}^{**} = \boldsymbol{V}_{\mathrm{d}}^{**} = \frac{\boldsymbol{V}_{\mathrm{u}}^{*} + \boldsymbol{V}_{\mathrm{d}}^{*}}{2}. \tag{9}$$

For simplicity, the above formulation is expressed in the non-conservative form, however, the actual computation is based on the conservative formalism taking the geometric conservation law (GCL) into account. [2]

3 GCIC+I

In the theory of the GCIC, the grid lines must be continuous on the interface. In this section, theoretical extension of the GCIC for discontinuous grid line connections is taken into account. In order to realize the present purpose, some high-order interpolation methods are incorporated into the GCIC. Namely, the GCIC with interpolation method (GCIC+I) are newly proposed. Firstly, the basic concept and solution procedures of the GCIC+I are shortly described. Then, two kinds of high-order interpolation method are introduced and their concrete implementations are explained in detail.

3.1 Basic Concept and Solution Procedures

Figure 2 shows the basic concept and strategy of the GCIC+I. As a premise, the adjacent sub-domains with 3D structured grids share the same 2D interface represented by gray color, but their grid points are not necessarily collocated on the same geometrical positions. (However, the four grid points at the corners of the interface are completely collocated.) The solution procedures are advanced through the following steps:

Step 1. Functional values on the physical space $\tilde{\mathrm{A}}\,/\,\tilde{\mathrm{B}}$ are mapped onto those of the computational space $\mathrm{A}\,/\,\mathrm{B}$: $\tilde{\mathrm{A}} \rightarrow \mathrm{A}\,/\,\tilde{\mathrm{B}} \rightarrow \mathrm{B}$.

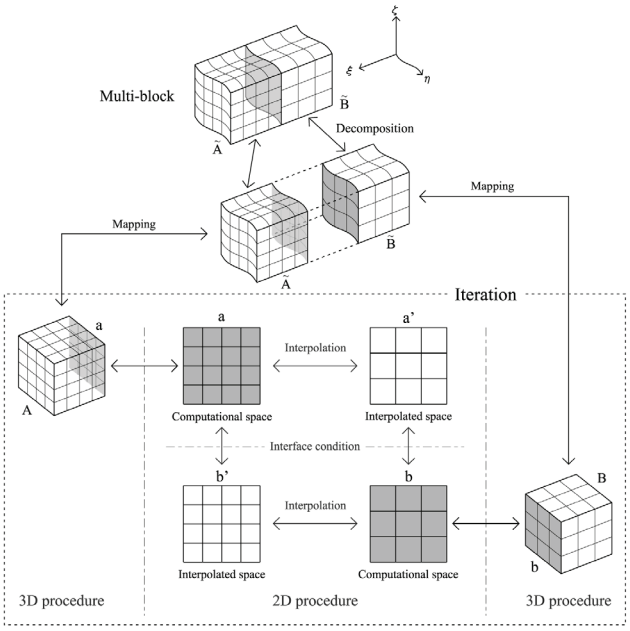

Fig. 2. Concept and strategy of multi-block computation using GCIC+I.

Step 2. The functional values on the computational space a/b are further interpolated to those on the interpolated space a'/b' which is defined by the computational space of the other side: $\mathrm{a} \to \mathrm{a}'/\mathrm{b} \to \mathrm{b}'$.

Step 3. The GCIC described in the previous section are employed between the computational space a/b and the interpolated space b'/a', which have the same positions each other: $\mathrm{a} \leftrightarrow \mathrm{b}'/\mathrm{b} \leftrightarrow \mathrm{a}'$.

Step 4. The governing equations are independently solved in the computational space of each sub-domain A/B, and the solutions are updated by a certain proper time integration scheme.

Step 5. The updated functional values on the computational space A/B are re-mapped onto those of the physical space $\tilde{\mathrm{A}}/\tilde{\mathrm{B}}$:

$\mathrm{A} \to \tilde{\mathrm{A}}/\mathrm{B} \to \tilde{\mathrm{B}}$.

In the actual computation, the procedures from step 2 to step 4 are iteratively solved in the time advancement. In the step 3, Eq. (6) is modified as follows:

$$\begin{aligned} \boldsymbol{L}_{\mathrm{u}} &= \underline{S}_{\mathrm{u}}^{-1}\left[\underline{S}_{\mathrm{d}}^{I}\boldsymbol{L}_{\mathrm{d}}^{I} + \underline{P}_{\mathrm{u}}^{-1}\left(\boldsymbol{D}_{\mathrm{d}}^{I} - \boldsymbol{D}_{\mathrm{u}}\right)\right], \\ \boldsymbol{L}_{\mathrm{d}} &= \underline{S}_{\mathrm{d}}^{-1}\left[\underline{S}_{\mathrm{u}}^{I}\boldsymbol{L}_{\mathrm{u}}^{I} + \underline{P}_{\mathrm{d}}^{-1}\left(\boldsymbol{D}_{\mathrm{u}}^{I} - \boldsymbol{D}_{\mathrm{d}}\right)\right]. \end{aligned} \tag{10}$$

where, the terms with a superscript " I " indicate the interpolated ones. Thus, in order to obtain the unknown characteristic amplitude variation vector $\boldsymbol{L}$ of the one side, the following three components, namely, interpolated characteristic amplitude variation vector $\boldsymbol{L}^{I}$, interpolated Jacobian matrix $\underline{S}^{I}$ and interpolated source vector $\boldsymbol{D}^{I}$ of the other side have to be prepared. Note that the interpolation is performed on 2D interface in 3D problem; generally, the interpolation dimensions are lower than the spatial dimensions of governing equations by one.

3.2 High-order Interpolation Method

As shown in Fig. 3, 2D interpolation strategy in the computational space is taken into account. In the bounded donor grids with uniform interval, the receiver point P is located arbitrarily. If the offset indices δ_η and δ_ζ can be known beforehand, functional values can be interpolated based on them from the donor points to the receiver point. In the present study, for consistency with a high-order spatial finite difference scheme, one of the following two kinds of the high-order 2D interpolation method is reasonably incorporated.

(a) Lagrange interpolation method:

For given set of n data points with functional values, there is only one smooth polynomial of degree n-1 passing through them all. The interpolation polynomial in the Lagrange form is given in a linear combination of the Lagrange basis polynomials, and is a function of class C^n anywhere within the bounded donor domain. While the construction and implementation are relatively easy, the high-order Lagrange interpolation has oscillating characteristics called as the Runge's phenomenon. In this study, the 1D Lagrange interpolation formula is extended to 2D:

$$f_L\left(\delta_\eta, \delta_\zeta\right) = \sum_k \sum_j L_j^n\left(\delta_\eta\right) L_k^n\left(\delta_\zeta\right) f_{j,k}, \tag{11}$$

where, L^n is the n-th order Lagrange basis polynomial, and $f_{j,k}$ and f_L are certain functional values of the donor point and receiver point respectively. When continuous n donor points are selected within $N(>n)$ data points, their domain is arranged so that the receiver point may be located at near its center as much as possible. However, one-sided treatments are reluctantly performed at the near boundaries of the data points.

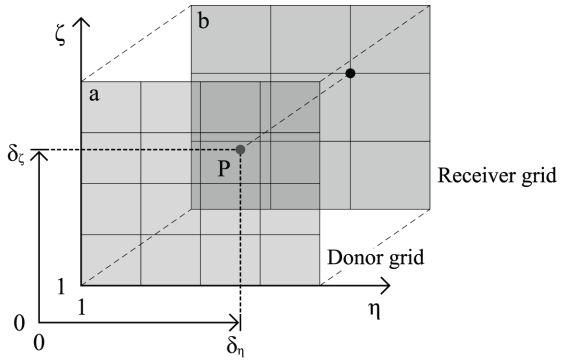

Fig. 3. 2D interpolation in computational space.

(b) B-spline interpolation method:

When certain functional values are given in a set of $N(>n)$ data points, a linear summation of some of the n-th order B-spline bases is taken into account to construct the n-th order B-spline function. The data points are divided by $N-n$ knot points to define local supports, where some of the non-zero B-spline bases exist. A smooth interpolating formula of class C^{n-2} can be constructed all over the domain, however, the local polynomials are changed on the knot points. If the knot point sequence is properly decided, the B-spline interpolation shows excellent characteristics with respect to numerical accuracy and robustness even in the high order of accuracy. However, the computational cost is more expensive than that of the Lagrange interpolation, because some band matrix manipulations are needed. In this study, the 1D B-spline interpolation formula is extended to 2D:

$$\begin{aligned} &f_B(\delta_\eta,\delta_\zeta)=\sum_m\sum_l c_{l,m}B_l^n(\delta_\eta)B_m^n(\delta_\zeta),\\ &\sum_m\sum_l c_{l,m}B_l^n(j)B_m^n(k)=f_{j,k}, \qquad (12)\\ &(j=1,\cdots,N_j,k=1,\cdots,N_k), \end{aligned}$$

where, B^n is the normalized n-th order B-spline basis, c is coefficient, and $f_{j,k}$ and f_B are certain functional values of the donor point and receiver point respectively.

3.3 Offset Index

In order to realize the interpolation procedures in the previous section, offset indices have to be known and prepared beforehand. By applying Eq. (11) or (12) to the physical coordinates of the grid points on the interface, these can be easily derived. If a relative position of the receiver point against the donor points is unchanged in terms of time, the following manipulations are performed only once at the beginning of the computation:

(a) Lagrange interpolation method:

$$\sum_k\sum_j L_j^n(\delta_\eta)L_k^n(\delta_\zeta)\begin{pmatrix}\boldsymbol{x}_{j,k}\cdot\boldsymbol{a}\\ \boldsymbol{x}_{j,k}\cdot\boldsymbol{b}\end{pmatrix}=\begin{pmatrix}\boldsymbol{x}_P\cdot\boldsymbol{a}\\ \boldsymbol{x}_P\cdot\boldsymbol{b}\end{pmatrix}, \qquad (13)$$

(b) B-spline interpolation method:

$$\begin{aligned} &\sum_m\sum_l\begin{pmatrix}a_{l,m}\\ b_{l,m}\end{pmatrix}B_l^n(\delta_\eta)B_m^n(\delta_\zeta)=\begin{pmatrix}\boldsymbol{x}_P\cdot\boldsymbol{a}\\ \boldsymbol{x}_P\cdot\boldsymbol{b}\end{pmatrix},\\ &\sum_m\sum_l\begin{pmatrix}a_{l,m}\\ b_{l,m}\end{pmatrix}B_l^n(j)B_m^n(k)=\begin{pmatrix}\boldsymbol{x}_{j,k}\cdot\boldsymbol{a}\\ \boldsymbol{x}_{j,k}\cdot\boldsymbol{b}\end{pmatrix}, \qquad (14)\\ &(j=1,\cdots,N_j,k=1,\cdots,N_k), \end{aligned}$$

where, linearly independent vectors $\boldsymbol{a}$ and $\boldsymbol{b}$ are introduced for avoiding a degeneration of the equations and are arbitrarily chosen, e.g., $\boldsymbol{a}=\boldsymbol{x}_{N_j,1}-\boldsymbol{x}_{1,1}$ and $\boldsymbol{b}=\boldsymbol{x}_{1,N_k}-\boldsymbol{x}_{1,1}$. The above non-linear equations can be easily solved with respect to the offset indexes δ_η and δ_ζ using the Newton-Raphson method.

4 Results and Discussion

In the following section, 2D viscous flows around a circular cylinder are solved for a validation of the GCIC+I. The inviscid and viscous flux derivatives of the Navier-Stokes equations are solved by the optimized 4th order penta-diagonal (OFOP) compact finite difference scheme suggested by Kim [3]. This scheme maintains a penta-diagonal Padé form, and has the maximum spatial resolution, optimizing dissipation and dispersion errors simultaneously. For the time integration, the low storage type of 2 step with 5 / 6 stage 4th order low-dissipation and low-dispersion Runge-Kutta (LDDRK) scheme proposed by Stanescu et al. [4] is used. This scheme increases numerical stability in the explicit time integration, and reduces dissipation and dispersion errors simultaneously. The 8th order tri-diagonal Padé type compact filter scheme proposed by Gaitonde et al. [5] is employed for a removal of high frequency aliasing errors which bring about numerical instabilities. The filter control parameter which relates to cut-off frequency is fixed as 0.495. As the boundary conditions, the Navier-Stokes characteristic boundary conditions (NSCBC) in curvilinear coordinates derived by Kim et al. [6, 7] are applied. In cases with the GCIC+I, the Lagrange or B-spline interpolation with 6th order of accuracy is additionally combined.

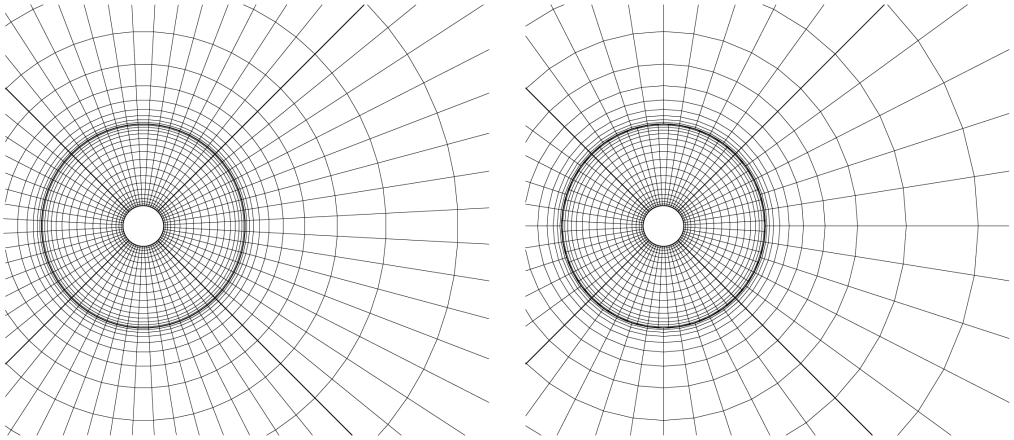

Fig. 4. Computational grids around a circular cylinder, without interpolation (left) and with interpolation (right).

Table 1. Details of validation test cases.

Case	Inner block	Outer block	R	Interpolation
N91-91	101*91	101*91	1	Non
L91-61	101*91	101*61	4/6	Lagrange
L91-46	101*91	101*46	3/6	Lagrange
L91-31	101*91	101*31	2/6	Lagrange
L91-16	101*91	101*16	1/6	Lagrange
B91-61	101*91	101*61	4/6	B-spline
B91-46	101*91	101*46	3/6	B-spline
B91-31	101*91	101*31	2/6	B-spline
B91-16	101*91	101*16	1/6	B-spline

Figure 4 shows computational grids around the circular cylinder of diameter 1.0. The computational domain is separated into two and four pieces in the radial and circumferential directions respectively, by the bold lines denoting the interface. Therefore, eight sub-domains exist in total. The inner sub-domain is from 0.5 to 2.5 in the radial direction and is 90 degrees extent in the circumferential direction. Similarly, the outer sub-domain is from 2.5 to 50 in the radial direction and is 90 degrees extent in the circumferential direction. In the present analysis, the number of circumferential grid points in the outer domain is focused as an important parameter to examine the performance of the theory, and changed according to Table 1. On the other hand, other grid parameters are fixed. For convenience, the ratio R between the number of circumferential grid points in the outer sub-domain $N_{\mathrm{out}}^{\theta}$ and that in the inner sub-domain N_{in}^{θ}, hereafter, 'Grid resolution consistency ratio', is defined as follows:

$$R := \frac{N_{\mathrm{out}}^{\theta} - 1}{N_{\mathrm{in}}^{\theta} - 1}. \tag{15}$$

Obviously, if R is nearly close to 1, the circumferential grid resolutions are almost the same between the inner and outer sub-domains. Conversely, if R is close to 0, those are considerably different.

The grid spacing is clustered near the wall boundary and the block interfaces in the radial direction with the minimum size of 0.02 in order to resolve dynamic flow variations resulting from the Kármán vortex sheets, and are coarsened gradually towards the outflow boundary in order to dump them. The computation has been continued until the non-dimensional time of $T \approx 225$. The time step size is determined by the CFL condition of the Courant number of 1.0, and the total iteration number is 275,000 steps.

Figure 5 shows instantaneous static pressure and streamwise velocity snapshots at the final step in L91-61 and L91-16. In L91-61, several flow characteristics, e.g., an attached boundary layer on the cylinder wall surface, a mixing layer of separated flows, and the Kármán vortex sheets behind the cylinder, can be clearly caught, however, in L91-16, dynamic ranges of these profiles are relatively narrow, and the Kármán vortex sheets are weakly generated. Especially, numerical oscillations are produced in the vicinity of the interfaces and propagate downstream. Figure 6 shows temporal behaviors of lift and drag coefficients in the Lagrange interpolation cases. In the first three cases, transient states are apparently different, however, similar amplitudes and frequencies are observed in the periodic states. On the other hand, in L91-16, the solution cannot properly reproduce the unsteady physical phenomena at all, the amplitude decays and the frequency decreases slightly.

Similarly, the instantaneous static pressure and streamwise velocity snapshots at the final step in B91-61 and B91-16 are shown in Fig. 7. Similar tendencies can be observed compared with the Lagrange cases, however, in B91-16, the Kármán vortex sheets are clearly generated, and numerical oscillations are not almost observed. These tendencies are contrastive to the solutions of L91-16. The temporal behaviors of the lift and drag coefficients in the B-spline interpolation cases are shown in Fig. 8. Apparently, the former two cases with high R value present similar evolution process into the periodic mode. In B91-31, the amplitude and frequency in the periodic mode are almost the same compared with the former two cases, however, transient time to the periodic mode is too long, because feedbacks from the downstream region to the upstream region are prevented by a considerable decrease of the grid resolution in the outer sub-domain. On the other hand, in B91-16, numerical errors in the vicinity of the interface grow up, and the solution overestimates the amplitude of the periodic mode compared with the other cases. However, in the calculations under the small R value of large inconsistency of grid resolutions, the B-spline interpolation is more robust and superior than the Lagrange interpolation. Furthermore, in order to discuss more quantitatively, a root mean square (RMS) value of the lift coefficients, a mean value of the drag coefficients and the Strouhal number are introduced and defined as follows:

$$\begin{aligned} \overline{C_L^2}^{1/2} &:= \sqrt{\frac{1}{T_2 - T_1}\int_{T_1}^{T_2} C_L^2(t)\,dt}, \\ \overline{C_D} &:= \frac{1}{T_2 - T_1}\int_{T_1}^{T_2} C_D(t)\,dt, \\ St &:= f\frac{d_0}{u_\infty} = \frac{1}{T}\frac{d_0}{u_\infty}. \end{aligned} \tag{16}$$

where, non-dimensional time from T=175 to T=225 (about 10 periods) is sampled for the estimation. In Eq. (16), d_0 and u_0 indicate the diameter and the uniform inflow velocity, and are both given as 1.0. Therefore, the Strouhal number means the frequency (reciprocal of the period) as a result. These above values in the all cases are summarized in Table 2. Based on the values in N91-91, those in the six cases of L91-61, L91-46, L91-31, B91-61, B91-46 and B91-31 are within an error range of 1 %, and these cases can reproduce the unsteady physical phenomena correctly. However, especially in L91-16, the error reaches to tens of percent, and the solution is considerably deteriorated. Consequently, tolerance of the grid resolution consistency ratio in the present validation tests is about $R \geq 1/3$. With less than this value, deterioration of the solution cannot be avoided, however, this tendency is smaller in the case with the B-spline interpolation than that with the Lagrange interpolation.

5 Conclusions

The generalized characteristic interface conditions (GCIC) are extended to the GCIC+I (GCIC with interpolation) by incorporating the high-order interpolation method. The main features of the present theory are not only permitting singularities of the grid connection on the interface but also changing grid resolutions in each sub-domain (block). In this article, the theoretical concept and mathematical procedures are described in detail. Furthermore,

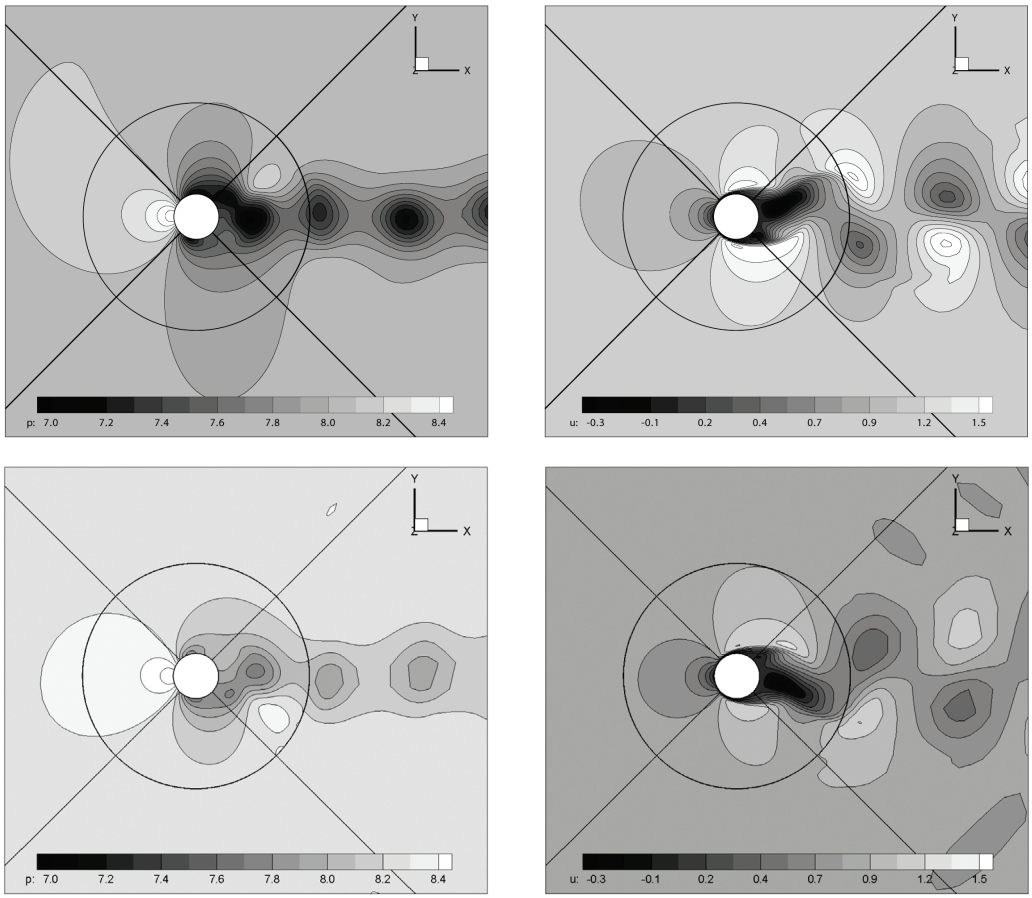

Fig. 5. Instantaneous profiles of static pressure (left) and streamwise velocity component (right) at final step, L91-61 (upper) and L91-16 (lower).

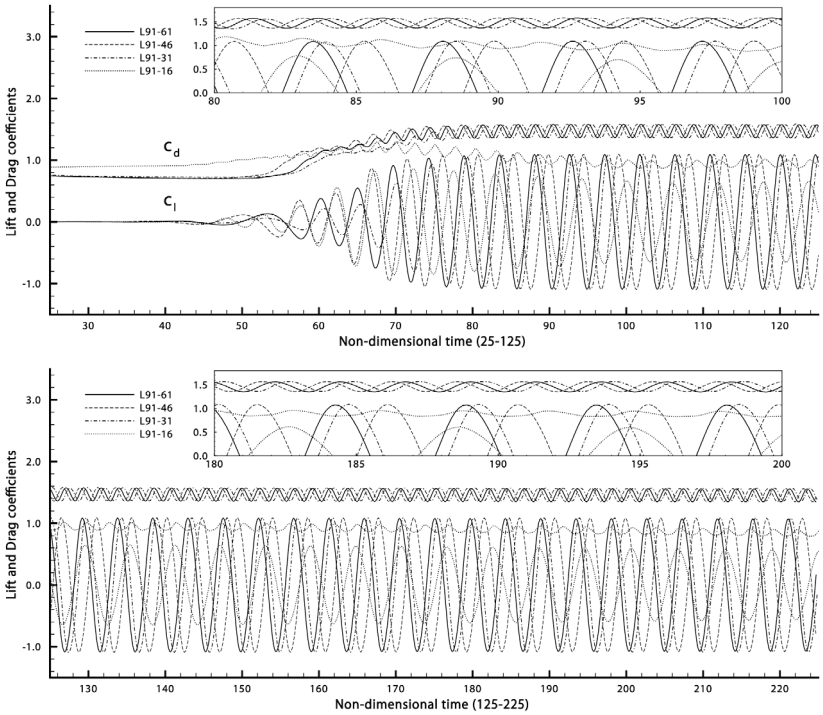

Fig. 6. Temporal behaviors of lift and drag coefficients in the Lagrange interpolation cases.

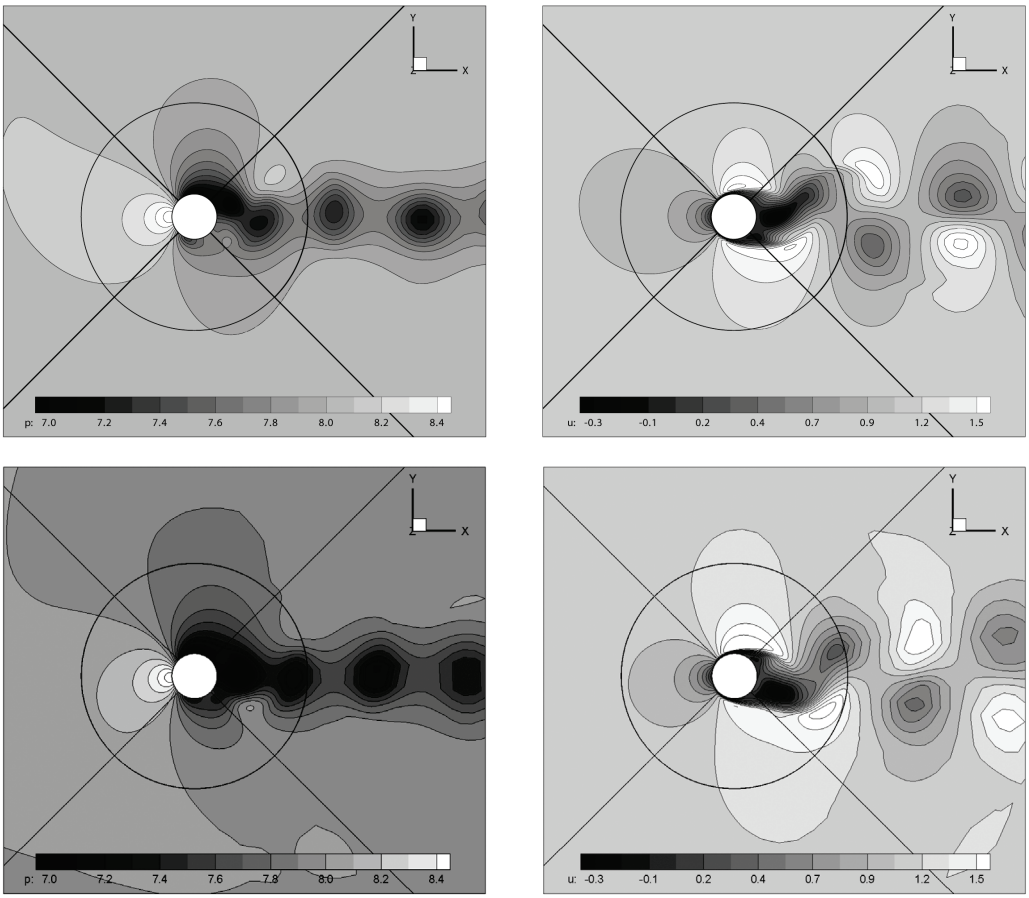

Fig. 7. Instantaneous profiles of static pressure (left) and streamwise velocity component (right) at final step, B91-61 (upper) and B91-16 (lower).

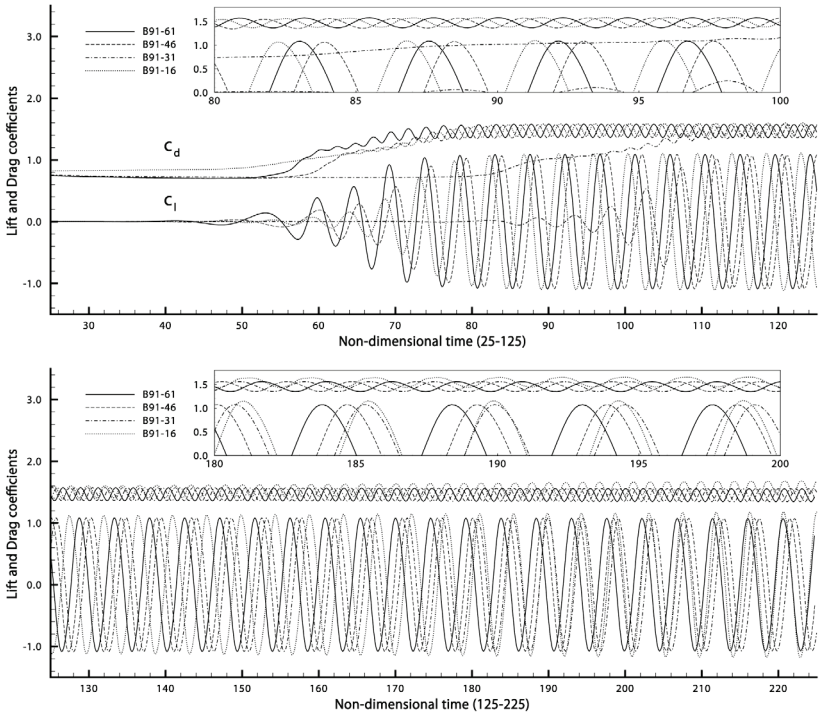

Fig. 8. Temporal behaviors of lift and drag coefficients in the B-spline interpolation cases.

Table 2. RMS values of lift coefficients, mean values of drag coefficients and the Strouhal numbers.

Case	$\overline{C_L^2}^{1/2}$	$\overline{C_D}$	St
N91-91	0.763	1.454	0.217
L91-61	0.760	1.458	0.217
L91-46	0.760	1.461	0.218
L91-31	0.773	1.471	0.218
L91-16	0.444	0.869	0.166
B91-61	0.755	1.456	0.217
B91-46	0.765	1.460	0.217
B91-31	0.763	1.458	0.218
B91-16	0.824	1.567	0.227

as a validation analysis, viscous flows around a circular cylinder are tested in detail by varying a grid parameter and kinds of interpolation methods. As a result, the authors have confirmed desirable functions of the GCIC+I, and proposed a guiding principle enhancing practicability and flexibility of the high-order multi-block computation on structured grids.

As high-order interpolation methods, the explicit Lagrange and B-spline interpolation methods are introduced and compared. Under a block connection with comparable tangential grid resolution, any large differences cannot be observed between the both methods by applying interpolation order of 6 (fixed in the present study), however, the later is more accurate and robust than the former under the extreme block connection with large grid resolution difference. According to our numerical tests, even if numerical instabilities are not caused by the interpolation operations, physical phenomena are not necessarily reproduced correctly depending on the grid resolution setting. Although the interface locations and the grid resolutions of the sub-domains are problem dependence, certain trade-offs exist in order to obtain accurate solutions.

The interpolation operations of the present theory are performed within the interface. As a result, the interpolation dimensions are lower than the spatial dimensions of the governing equations by one. Therefore, the present theory may be functioning well in general 3D problems with complex geometry rather than simple 2D problems. Further comprehensive study needs to be made to investigate the practical utilities.

References

[1] Sherer, S. and Scott, J., High-order compact finite-difference methods on general overset grids, *J. Comput. Phys.*, Vol. 210, pp. 459-496, 2005.

[2] Sumi, T., Kurotaki, T. and Hiyama, J., Generalized characteristic interface conditions for high-order multi-block computation, *Int. J. Comput. Fluid Dynam.*, Vol. 21, pp. 335-350, 2007.

[3] Kim, J., Optimized boundary compact finite difference schemes for computational aeroacoustics, *J. Comput. Phys.*, Vol. 225, pp. 995-1019, 2007.

[4] Stanescu, D. and Habashi, W., 2N-storage low dissipation and dispersion Runge-Kutta schemes for computational aeroacoustics, *J. Comput. Phys.*, Vol. 143, pp. 674-681, 1998.

[5] Gaitonde, D. and Visbal, M., Padé-type higher-order boundary filters for the Navier-Stokes equations, *AIAA J.*, Vol. 38, pp. 2103-2112, 2000.

[6] Kim, J. and Lee, D., Generalized characteristic boundary conditions for computational aeroacoustics, *AIAA J.*, Vol. 38, pp. 2040-2049, 2000.

[7] Kim, J. and Lee, D., Generalized characteristic boundary conditions for computational aeroacoustics, part 2, *AIAA J.*, Vol. 42, pp. 47-55, 2004.

Copyright Statement